Structural, Transport, and Magnetic Properties of the $Nd_{1-x}A_xTiO_3$ (A = Ca, Sr, Ba) System Where $0 \leq x \leq 1$

C. Eylem,* H. L. Ju,† B. W. Eichhorn,*,¹ and R. L. Greene†,¹

Center for Superconductivity Research, Department of Chemistry and †Department of Physics, University of Maryland, College Park, Maryland 20742

A series of perovskite $Nd_{1-x}A_xTiO_3$ (A = Ca, Sr, Ba) compounds has been prepared by the dc-arc melting technique in the composition range $0 \leq x \leq {\sim}1.0$. The substitution of Sr and Ba in $NdTiO_3$ results in structural phase transitions from orthorhombic (*Pbnm*) to cubic (*Pm3m*). The $Nd_{1-x}Ca_xTiO_3$ series remains orthorhombic throughout the range studied. Low field magnetic susceptibility measurements and remanent magnetic moment studies suggest that the Ti sublattice in the insulating $Nd_{1-x}A_xTiO_3$ compounds ($0 \leq x \leq {\sim}0.2$) orders as canted antiferromagnets. The $Nd_{1-x}A_xTiO_3$ compounds show compositionally dependent metal–insulator transitions that coincide with the disappearance of the magnetic ordering. The correlations between the structure and transport properties are discussed in terms of the Ti–O–Ti angle and Ti–O bond distance. The perovskite tolerance factor, t, is also shown to be a useful parameter to sort insulating and metallic phases in these compounds. © 1995 Academic Press, Inc.

INTRODUCTION

Despite the large number of metallic and insulating perovskite oxides, there is still a general lack of understanding of the factors affecting the transport properties in perovskite-related materials. Band calculations (1, 2) can sometimes describe properties in specific compounds but require detailed knowledge of structural parameters and are not applicable to large classes of materials. Recently, ionic models such as the Zaanen–Sawatzky–Allen (ZSA) model (3) have been designed to sort compounds based on experimental electronic parameters (i.e., ionization potentials, electron affinities). According to ZSA theory (3), insulating compounds arising from strong correlations between d electrons can be categorized into two classes, Mott–Hubbard (M–H) and charge transfer (CT) insulators. In the former case, the band gap is between the d-electron states (upper and lower Hubbard bands), whereas in the latter, the gap is between the

¹ To whom correspondence should be addressed.

oxygen-like filled state and the unoccupied d-like upper Hubbard band. In the ZSA scheme, the early transition metal perovskites (i.e., $RTiO_3$, RVO_3, where R = rare-earth) are in the Mott–Hubbard class.

The d^1-$RTiO_3$ (Ti^{3+}) phases represent an interesting series of compounds in which the structure, transport, and magnetic properties are influenced by the size and the electronegativity of the rare-earth ions (4, 5). The $RTiO_3$ compounds adopt the orthorhombic $GdFeO_3$ structure (space group *Pbnm*) and are all insulating. The larger rare-earth ions form antiferromagnetic compounds, whereas the smaller rare-earth ions form ferromagnetic phases.

The structure and properties of the $RTiO_3$ compounds can be varied by chemical substitution of A^{2+} for R^{3+}, forming solid solutions of general formula, $R_{1-x}A_xTiO_3$. For instance, Sr^{2+} and Ba^{2+} substitution in $LaTiO_3$ results in orthorhombic (*Pbnm*)-to-cubic (*Pm3m*) and insulator-to-metal transitions and quenches the antiferromagnetic ordering (6–9). Interestingly, the more orthorhombically distorted $YTiO_3$ compound displays insulator–metal transitions and quenched ferromagnetism when Y^{3+} is replaced by Ca^{2+} (35%) (10). The structure and properties of the other Ti-based systems such as $R_{1-x}Ba_xTiO_3$ (R = La, Nd, Gd, Er, Y) (6), $Nd_{1-x}Ca_xTiO_3$ (11), and $Ce_{1-x}A_xTiO_3$ (A = Sr, Ba) (12) have also been the subject of recent studies. It has been suggested that metal–insulator transitions in the titanates can be well described by a conventional Fermi liquid model (7, 11, 13). In contrast, some authors (14) have suggested that the metal–insulator transitions in the $R_{1-x}A_xVO_3$ vanadate perovskites (V^{3+}, d^2) are of an Anderson type (15).

A detailed understanding of the metal–insulator transitions in these class compounds will require thorough experimental and theoretical studies of many different systems. Through our studies, we are examining the interrelationship of structure, magnetism, and metal–insulator transitions in the perovskite $R_{1-x}A_xMO_3$ (R = rare-earth; A = alkaline-earth; M = Ti, V) compounds. In this paper, we report a detailed study of the Nd_{1-x}

A_xTiO_3 perovskites, where A = Ca, Sr, Ba, that display such metal–insulator transitions. The insulating $Nd_{1-x}A_xTiO_3$ compounds show weak ferromagnetic moments due to canted antiferromagnetic ordering. The metal–insulator transitions in these materials appear to be related to the magnetic ordering. We discuss the relationships between the structure and properties in terms of the Ti–O bond distance and Ti–O–Ti angle.

EXPERIMENTAL SECTION

A. Sample Preparation

$CaTiO_3$ was synthesized by heating TiO_2 (99%) and $CaCO_3$ (99.98%) in air at 1000°C for 24 hr with one intermediate grinding. $SrTiO_3$ (99.9%) and $BaTiO_3$ (99.9%) were purchased from CERAC. Solid solutions of $Nd_{1-x}A_xTiO_3$ ($0 \leq x \leq 1$) where A = Ca, Sr, Ba were prepared by arc-melting pelletized ~1% oxygen-deficient mixtures of predried $ATiO_3$, predried Nd_2O_3 (99.9%), and TiO_2 and Ti (99.5%). The pelletized mixtures and a zirconium metal button were placed on a water-cooled copper hearth inside an arc furnace that was evacuated and purged with gettered Ar (UHP) gas several times before the reaction. Samples were fired several times with repetitive turnings. Before each pellet was fired, the Zr button was melted in order to purify the atmosphere inside the furnace. The resulting phases were then pulverized in a percussion mortar, finely ground, and analyzed by powder X ray diffraction (XRD). Each sample was prepared and characterized at least twice. The synthesis was found to be highly reproducible. All single-phase samples were stored in a Vacuum Atmospheres dry box to prevent oxidation.

B. Sample Characterization

X ray diffraction data were collected at 25°C on a modified Phillips XRG 2000 diffractometer (CuK_α radiation) interfaced with a RADIX databox and MDI Software System. Cell refinement calculations were performed on all data collected between $20° < 2\theta < 70°$ and were corrected for sample displacement and zero-point error.

Oxygen contents were determined by thermogravimetric analysis (TGA). Large samples (~200 mg) were loaded into platinum boats and heated in air at 900°C for 12 hr resulting in light blue powders. The oxygen contents were calculated from the weight gains upon oxidation. It was assumed that the final oxidation state of Ti in the oxidized samples was +4. The uncertainty of the measurements was checked with a reference oxidation process where Ti metal was oxidized to TiO_2. The expected oxygen uptake was determined with a $\leq 1\%$ error.

Tolerance factors, t ($t = (r_A + r_O)/\sqrt{2} (r_B + r_O)$, where r_A and r_B are the average ionic radii at the A and B sites,

respectively, and r_O is the ionic radius of oxygen), were calculated using ionic radii of Shannon (16) appropriate to 6-fold Ti–O and 12-fold A–O coordinations. Twelve-coordinate radii for Y^{3+} were estimated based on the standard 11% increase from nine-coordinate radii for other rare-earth ions.

C. Property Measurements

Magnetic susceptibilities of the $Nd_{1-x}A_xTiO_3$ compounds were measured by using a Quantum Design SQUID magnetometer at applied fields of 50 G–35 kG. All samples were screened for superconductivity down to 4 K by low field dc susceptibility. The remanent moments were measured with zero field measurements. The samples were cooled from room temperature to 5 K in a magnetic field of 35 kG. The field was then turned off at 5 K and the magnetization was measured as the samples were warmed. The magnetic ordering temperatures were determined by taking the derivative of the inverse susceptibility ($d\chi^{-1}/dT$) where the maximum was chosen as an ordering temperature.

Resistivity measurements were made by using a standard four-probe technique. Arc melted $Nd_{1-x}A_xTiO_3$ (A = Ca, Sr) samples were cut into rectangular blocks (typically $1.5 \times 0.5 \times 0.3$ mm) and polished. Care was taken to avoid pieces containing cracks. Au wires were attached on samples with silver paste. Samples were not annealed prior to resistivity measurements. Contact resistances were less than 30 ohms.

The $Nd_{1-x}Ba_xTiO_3$ samples were masked and briefly cleaned in an Ar plasma. Then ca. 300–500 Å of Au were sputtered onto the samples. Contacts (Cu wires) were then made to the Au/Ti contacts with silver paste, and the samples were annealed under 5% H_2 in Ar at 180°C for 12 hr. Contact resistances were less than 10 ohms.

RESULTS

A. Synthesis and Structure

Single-phase substitutional solid solutions of general formula $Nd_{1-x}A_xTiO_3$ (A = Ca, Sr, Ba) were prepared throughout the range $0 \leq x \leq 1$ for Sr, Ba and $0 \leq x \leq 0.8$ for Ca. The oxygen stochiometry of the $Nd_{1-x}A_xTiO_3$ samples were closely monitored by thermogravimetric analysis. The results are consistent with an oxygen stochiometry 3.00 (± 0.03) for all samples investigated. Due to the nature of sample preparation (a fast quenching from > 2000°C), the observed symmetry changes may not represent equilibrium conditions.

$Nd_{1-x}A_xTiO_3$ structural phase transitions for the alkaline-earth series are summarized in Fig. 1. The substitution of Nd^{3+} by the large ions Sr^{2+} and Ba^{2+} results in
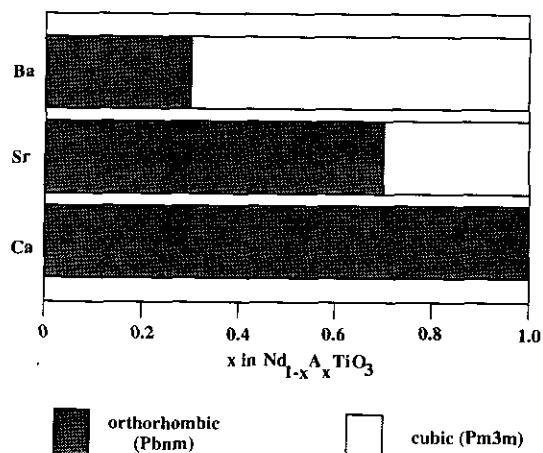
EYLEM ET AL.

orthorhombic
(Pbnm)   cubic (Pm3m)

FIG. 1. Structural phase diagram of the $Nd_{1-x}A_xTiO_3$ phases where A = Ca, Sr, Ba.

orthorhombic-to-cubic phase transitions, whereas the $Nd_{1-x}Ca_xTiO_3$ compounds remain orthorhombic for all values of x. The structural phase transitions in the Ba and Sr systems might involve tetragonal intermediates (17). Each system will be described individually below.

$NdTiO_3$ forms extensive substitutional solid solutions with $BaTiO_3$ in the range $0 \le x \le 1$. The cell parameters as a function of x are plotted in Fig. 2a. The details of the structural phase transitions have been discussed elsewhere (6).

The substitution of Nd by the smaller alkaline-earth Sr in $NdTiO_3$ ($Nd_{1-x}Sr_xTiO_3$) results in the same phase transitions as the $Nd_{1-x}Ba_xTiO_3$ system. Figure 2b displays the unit cell parameters of the $Nd_{1-x}Sr_xTiO_3$ phases as a function of x. The orthorhombic perovskite region in the $Nd_{1-x}Sr_xTiO_3$ system persists over a composition range $0 \le x \le 0.3$. At $x \approx 0.3$, the a and b cell parameters

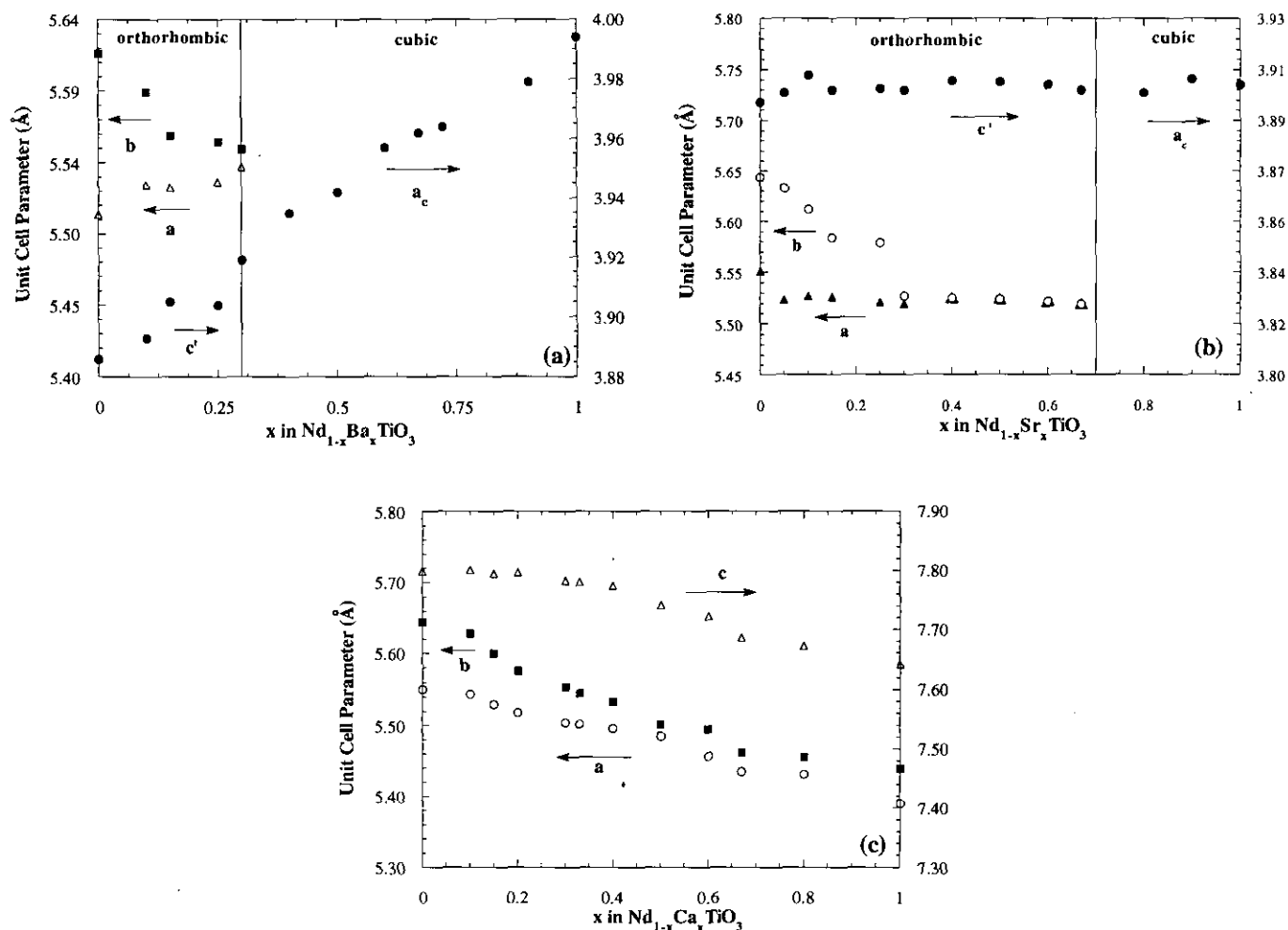**FIG. 2.** Unit cell parameters as a function of x for (a) $Nd_{1-x}Ba_xTiO_3$. In the orthorhombic region, the c lattice parameter (c_0) is divided by 2. $c' = c_0/2$. (b) $Nd_{1-x}Sr_xTiO_3$. In the orthorhombic region, $c' = c_0/2$. Unit cell parameters in the composition range $0.3 < x < 0.7$ are plotted as orthorhombic although a and b parameters are indistinguishable from the cell refinements. (c) $Nd_{1-x}Ca_xTiO_3$.

converge and the XRD profiles in the composition range $0.3 < x < 0.7$ could be refined either with double cubic symmetry ($a = 2a_p$) or tetragonal symmetry ($a \approx a_p/\sqrt{2}$, $c \approx 2a_p$). Attempts to refine the data in this composition range with orthorhombic symmetry always resulted in identical a and b cell parameters (i.e., a tetragonal cell). However, linewidth analyses showed a continuous increase in the diffraction peak widths from the $x = 0.7$ to $x = 0.3$ samples suggesting that the structures may not cubic or tetragonal (all peaks are broadening). These data seem to indicate that the phases in this region are (barely) orthorhombic even though our cell refinements suggest otherwise. We can exclude an *Ibmm* type structure due to the persistence of the 003 and 113 reflections throughout this range. Neutron diffraction and/or single crystal X ray studies are needed to fully understand this behavior. Beyond $x \geq 0.7$, the $Nd_{1-x}Sr_xTiO_3$ phases adopt the prototypical simple cubic perovskite structure (space group $Pm3m$).

$NdTiO_3$ also forms substitutional solid solutions with $CaTiO_3$ ($Nd_{1-x}Ca_xTiO_3$) throughout the range $0 \leq x \leq 0.8$. These compounds adopt the orthorhombic $GdFeO_3$ structure (space group *Pbnm*) for all x. Figure 2c shows the unit cell parameters of the $Nd_{1-x}Ca_xTiO_3$ samples as a function of x. The unit cell parameters a, b, and c are observed to decrease gradually as the $CaTiO_3$ compound ($x = 1.0$) is approached.

B. Transport Properties

Resistivity (ρ) measurements were carried out between 300 and 4 K. Plots of log ρ vs $1/T$ for $NdTiO_3$ and $Nd_{0.9}Ca_{0.1}TiO_3$ reveal semiconducting behavior that cor-
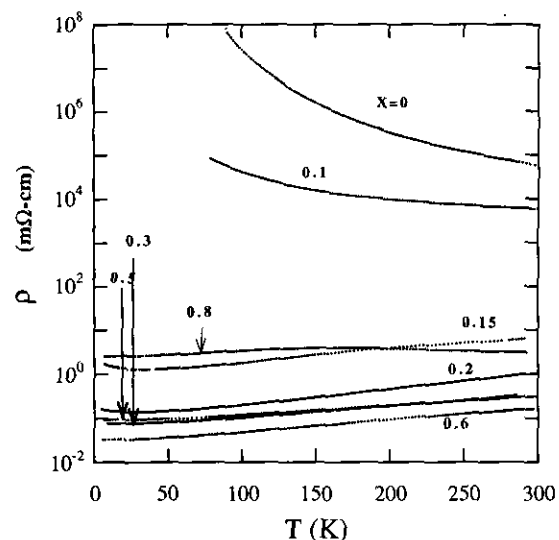
FIG. 4.   Plots of resistivity versus temperature for the $Nd_{1-x}Ca_xTiO_3$ compounds in the composition range $0 \leq x \leq 0.8$.

responds to band gaps of 0.16 and 0.05 eV, respectively (see Fig. 3). The measured $NdTiO_3$ band gap is in good agreement with the band gap measured by reflectivity data (0.16 eV) (18). The substitution of Nd by Ca decreases the resistivity and an insulator–metal transition occurs at $x \approx 0.15$. The resistivity vs temperature plots for compositions $0 \leq x \leq 0.8$ are shown in Fig. 4. The $x = 0.15$ sample shows metallic temperature dependence with a rather high resistivity suggesting that it resides near the metal–insulator boundary for the Nd-rich portion of the $Nd_{1-x}Ca_xTiO_3$ series. The $x = 0.15$ and 0.2 samples show upturns at low temperatures which may originate from localization effects associated with the observed remanent moments (see Section C). The $x = 0.6$ sample has the lowest resistivity with a value of 1.5 × 10^{-4} Ω-cm at 300 K. The resistivities of the samples ($x > 0.6$) increase as the band insulator $CaTiO_3$ ($x = 1.0$) is approached. We have not investigated the metal–insulator transition in the Ca-rich samples.

The transport properties of the $Nd_{1-x}Sr_xTiO_3$ samples are quite similar to the $Nd_{1-x}Ca_xTiO_3$ system and are shown in Fig. 5. The insulator–metal transition occurs at $x \approx 0.2$ with the lowest resistivities ($\sim 10^{-4}$ Ω-cm) found for $x = 0.5$ and 0.6 samples. A similar upturn at low temperatures is observed for the metallic $x = 0.2$ sample.

Four-probe resistivity measurements in the $Nd_{1-x}Ba_xTiO_3$ system were performed on gold-sputtered irregularly shaped pellets. Therefore, the precise resistivities were not measured. The representative plots of the relative resistance (R/R_{298}) versus T are shown in Fig. 6 for $Nd_{0.9}Ba_{0.1}TiO_3$ and $Nd_{0.4}Ba_{0.6}TiO_3$. Metallic conductivity in the less orthorhombically distorted $Nd_{1-x}Ba_xTiO_3$ se-
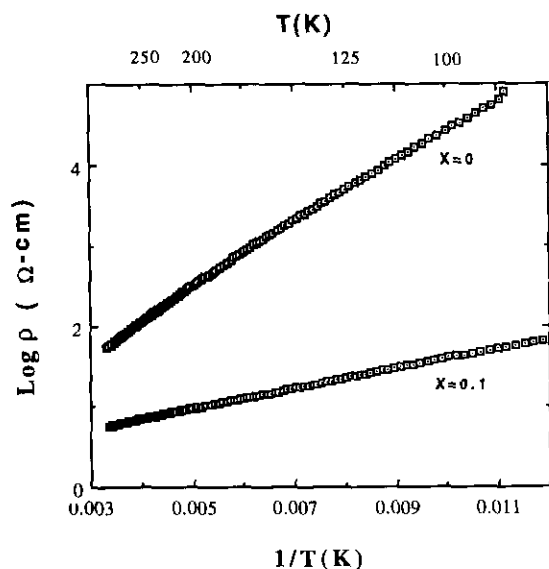

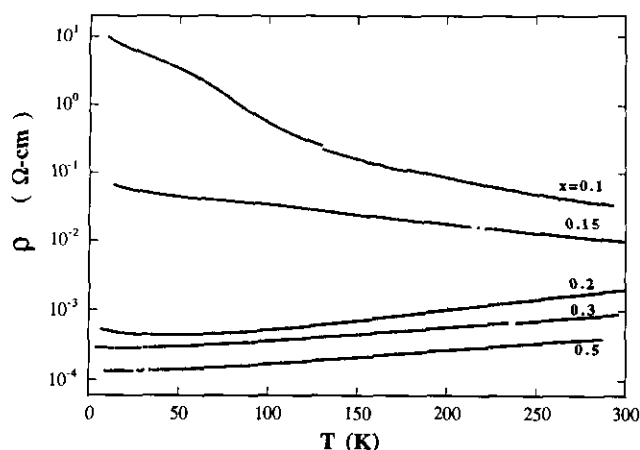FIG. 3.   Plots of log resistivity versus inverse temperature for Nd TiO_3 ($x = 0$) and $Nd_{0.9}Ca_{0.1}TiO_3$ ($x = 0.1$).

FIG. 5. Plots of resistivity versus temperature for the $Nd_{1-x}Sr_xTiO_3$ compounds in the composition range $0 < x \leq 0.5$.

ries appears at $x \leq 0.1$ and persists in the composition range $\sim 0.1 \leq x < 0.72$. The disappearance of metallic conductivity takes place at $x \approx 0.72$; beyond which semiconducting behavior is observed.

C. Magnetic Properties

The magnetic susceptibilities of the $Nd_{1-x}A_xTiO_3$ samples where $A = Ca$, Sr, Ba were measured between 4 and 300 K at an applied field of 1000 Gauss. Plots of their inverse susceptibilities (χ^{-1}) versus temperature are shown in Fig. 7. The susceptibilities of the $Nd_{1-x}A_xTiO_3$ phases are dominated by the magnetic Nd^{3+} ions $(4f^3)$ and display Curie–Weiss paramagnetism at high temperatures.

Magnetic ordering is observed at low temperatures for compositions $0 \leq x \leq 0.2$ for Ca and Sr and $0 \leq x \leq 0.15$ for Ba as shown in Fig. 8. The deviations from Curie–Weiss behavior at low temperatures are suggestive of weak magnetic ordering. Because magnetization is not observed for paramagnetic materials in the absence of a field, any remanent moment measured at zero field in a field-cooled experiment can be attributed to magnetic ordering. In this way, one can separate the paramagnetic Nd^{3+} moments from the weak ferromagnetic moments of the Ti^{3+} sublattice. The results are shown in Fig. 9 for samples in the composition region $0 \leq x \leq 0.2$. The Ti remanent moments were calculated by using the equation $M = NM_o$ where M is the total saturated moment at 5 K (see Fig. 9), N is the number of Ti^{3+} ions per unit volume, and M_o is the net ferromagnetic moment of Ti. The Ti ferromagnetic moment in $NdTiO_3$ was calculated to be $\sim 10^{-2}$ μ_B/Ti. The $x = 0.1$ members of the $Nd_{1-x}A_xTiO_3$ solid solutions have slightly higher Ti moments than the parent $NdTiO_3$. However, the magnitudes of these moments are quite small compared to the expected moment

for Ti^{3+}. For instance, the Ti^{3+} moment in $YTiO_3$ is 0.84 μ_B (19). The source of these weak ferromagnetic moments are probably due to canted antiferromagnetic ordering of the Ti sublattice as observed in $LaTiO_3$ (20). The approximate ordering temperature dependence on alkaline-earth (A) concentration is shown in the inserts of Fig. 9. It is seen that the ordering temperature generally decreases with increasing A concentration. $Nd_{0.95}Sr_{0.05}TiO_3$ is an exception with an ordering temperature slightly higher than $NdTiO_3$. The samples with $x > 0.15$ for Ba and $x > 0.2$ for Ca and Sr have no remanent moments within experimental error.

DISCUSSION

The structural transitions in the $Nd_{1-x}A_xTiO_3$ series are governed by the size of the alkaline earth ions, A^{2+}. The large Ba^{2+} ion induces a transformation to simple cubic symmetry at low x, whereas the small Ca^{2+} ion renders orthorhombic phases for all x. The exact concentrations at which the transformations to cubic symmetry for the Ba and Sr series are difficult to determine from powder X ray data. The X ray data can be refined on tetragonal or double cubic $(a = 2a_p)$ cells in the compositional regions close to the simple cubic structures. However, peak width analyses suggest that orthorhombic symmetry is maintained up to the $Pm3m$ regions. Similar problems of determining the correct crystal systems and space groups were encountered for the $LaTiO_3$ (21), $LaVO_3$ (22), and $Ca_{1-x}Sr_xTiO_3$ (23) systems. The subtleties in the structural phase transitions do not appear to have a significant affect on the magnetic or transport properties of these materials.
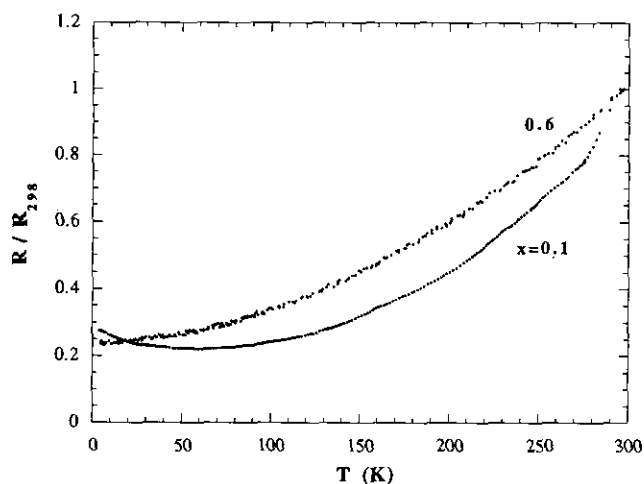

FIG. 6. Representative plot of relative resistance versus temperature for the $Nd_{0.9}Ba_{0.1}TiO_3$ ($x = 0.1$) and $Nd_{0.4}Ba_{0.6}TiO_3$ ($x = 0.6$) compounds.
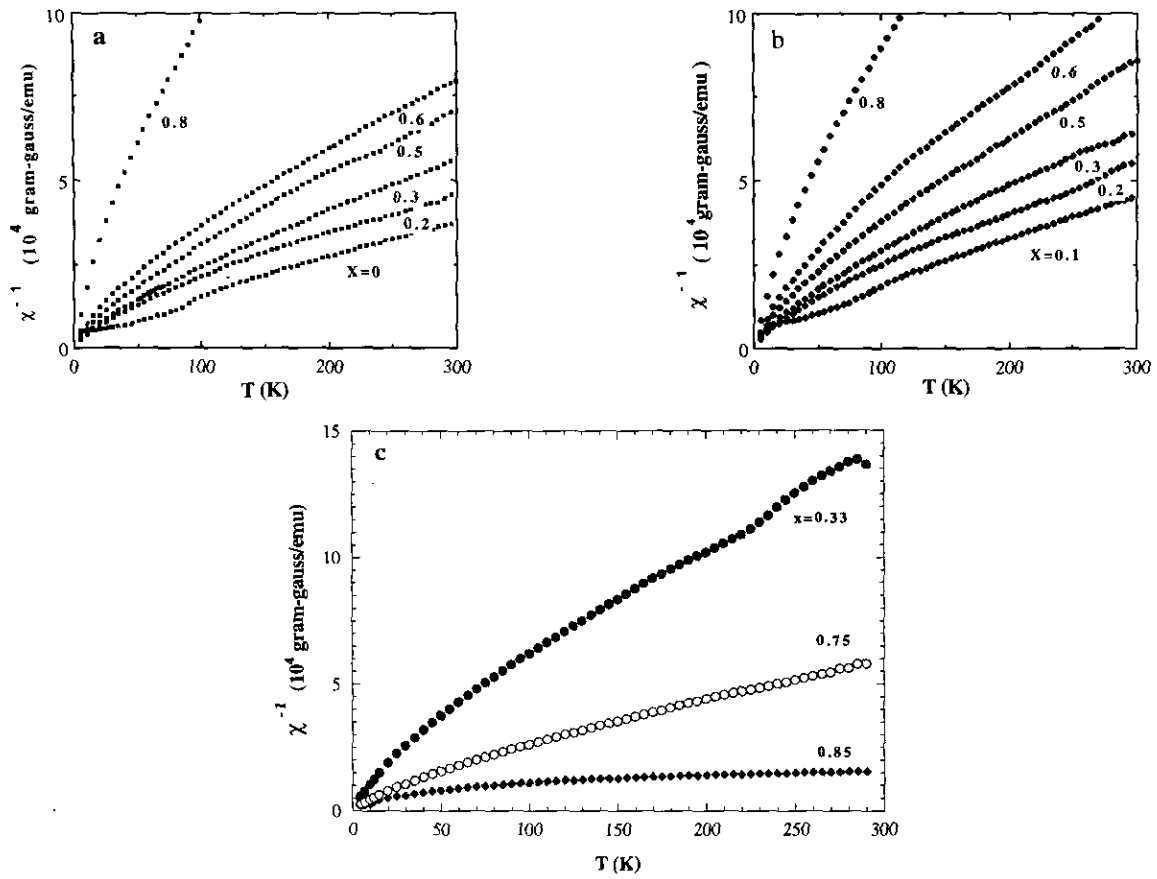
FIG. 7. Plots of inverse magnetic susceptibility (χ^{-1}) versus temperature at 1000 Oe for (a) $Nd_{1-x}Ca_xTiO_3$, (b) $Nd_{1-x}Sr_xTiO_3$, (c) $Nd_{1-x}Ba_xTiO_3$.
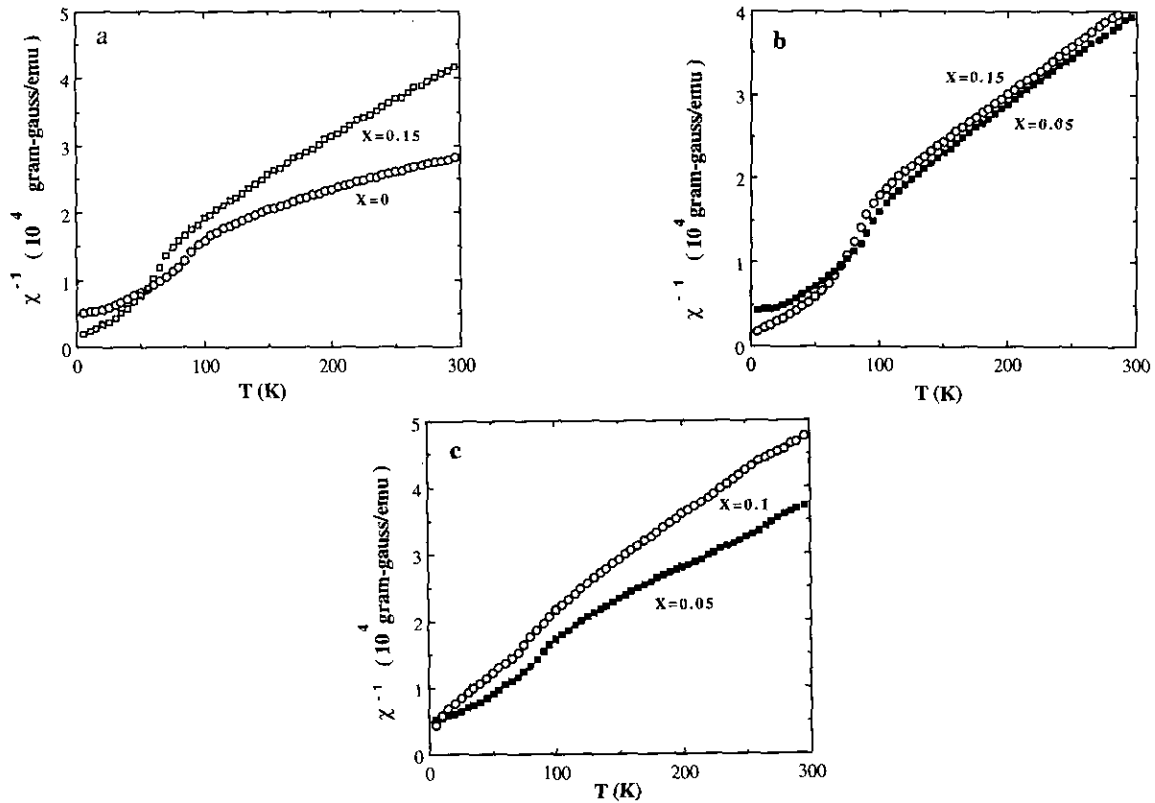

FIG. 8. Plots of inverse magnetic susceptibility versus temperature at an applied field of 50 Oe for (a) $Nd_{1-x}Ca_xTiO_3$ (x = 0 and 0.15), (b) $Nd_{1-x}Sr_xTiO_3$ (x = 0.05 and 0.15), (c) $Nd_{1-x}Ba_xTiO_3$ (x = 0.05 and 0.1).
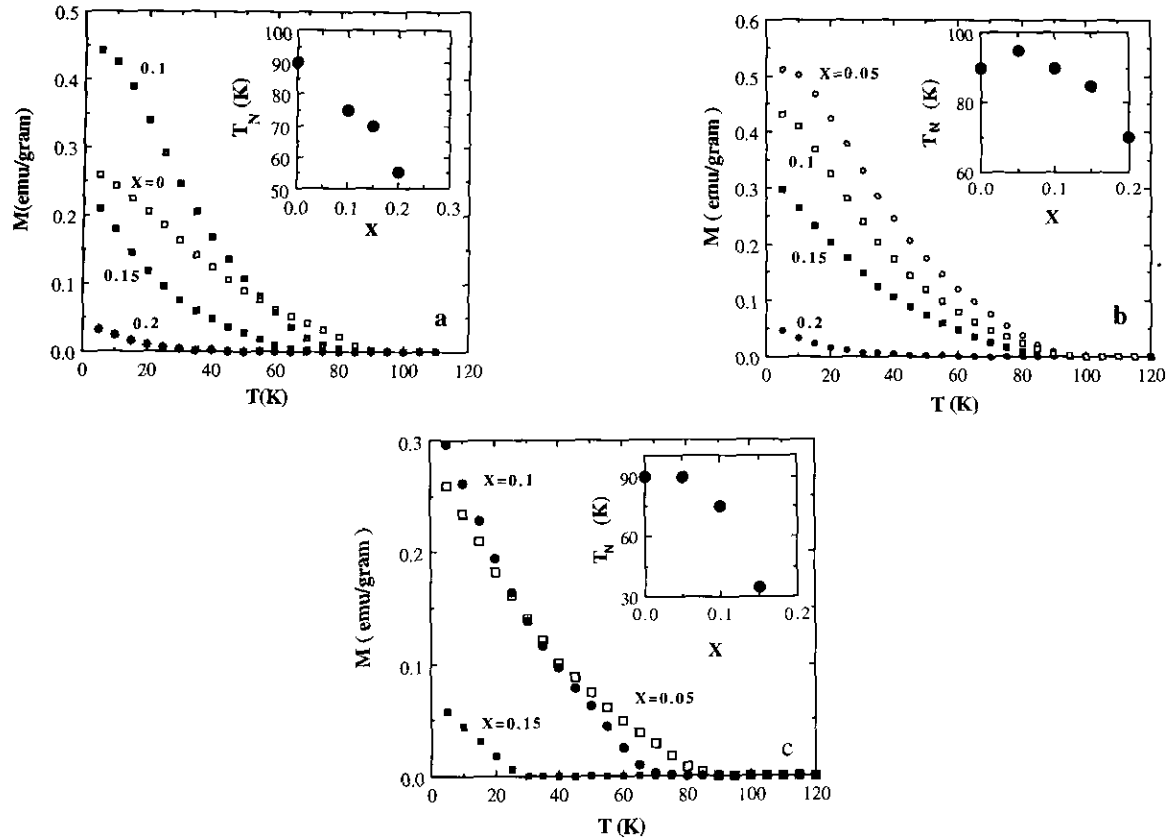
FIG. 9. Plots of magnetization versus temperature in the composition range $0 \le x \le 0.2$ for (a) $Nd_{1-x}Ca_xTiO_3$, (b) $Nd_{1-x}Sr_xTiO_3$, (c) $Nd_{1-x}Ba_xTiO_3$. The samples were cooled down in 3.5 T to establish the saturation of magnetization. Then, the magnetization was measured by warming the samples in a zero field. Inserts: Magnetic ordering temperature as a function of x for the samples $0 \le x \le 0.2$.

The $Nd_{1-x}A_xTiO_3$ phases where A = Ca, Sr, Ba display magnetic ordering at low temperatures and Curie–Weiss paramagnetism at high temperatures for compositions $0 \le x \le$ ~0.2. The parent $NdTiO_3$ compound was reported to be paramagnetic between room temperature and 4 K based on magnetic susceptibility and neutron diffraction studies (24, 25). However, our low field magnetic susceptibility measurements (50 Gauss) and remanent moment studies suggest that $NdTiO_3$ orders antiferromagnetically with an ordering temperature of 90 K. Due to the striking similarities in the susceptibility curves and observed magnetic moments between these compounds and $LaTiO_3$ (20), we assume that the Nd sublattice remains paramagnetic at all temperatures in our analyses. The weak remanent moments (~10^{-2} μ_B) and the relatively high ordering temperatures (~90 K) are inconsistent with Nd^{3+} ordering. Therefore, we attribute the weak ferromagnetism in the $Nd_{1-x}A_xTiO_3$ ($0 \le x \le$ ~0.2) samples to a canted antiferromagnetic ordering of the Ti sublattice. Because this ordering was not detected in the neutron diffraction study of $NdTiO_3$ (25), it is possible that the observed magnetic behavior is due to a magnetic spin glass. Interestingly, the Ti (III) sublattice orders antiferromagnetically in $LaTiO_3$ (20) and $CeTiO_3$ (26) as

well but at higher temperatures (125 and 115 K, respectively). $CeTiO_3$ also displays an additional magnetic anomaly below 60 K which has been attributed to Ce ordering. We did not see any additional magnetic anomalies in our samples.

The metallic $Nd_{1-x}Ca_xTiO_3$ ($0.15 \le x \le 0.2$), $Nd_{0.8}Sr_{0.2}TiO_3$, and $Nd_{0.9}Ba_{0.1}TiO_3$ samples exhibit upturns in resistivities at approximately the same temperatures as the onset of antiferromagnetic ordering. For instance, the magnetic ordering temperatures of the $Nd_{0.9}Ba_{0.1}TiO_3$ (~90 K) and $Nd_{0.8}Sr_{0.2}TiO_3$ (~70 K) samples are approximately the same as the upturn temperatures (see Figs. 5, 6, 9b and 9c). All metallic $Nd_{1-x}A_xTiO_3$ samples with weak magnetic moments show upturns in resistivities suggesting that the upturns are caused by localization effects associated with magnetic ordering. More detailed studies (e.g., magneto-resistance) are needed to reveal the nature of these localization effects. Resistivity upturns at low temperatures have also been observed in materials such as $CeTiO_3$ and $LaTiO_{3+\delta}$ which have ferromagnetic spin structures (26, 27).

By constructing a three-dimensional phase diagram similar to that of Tokura (28), we have summarized the electronic and magnetic properties of the perovskite
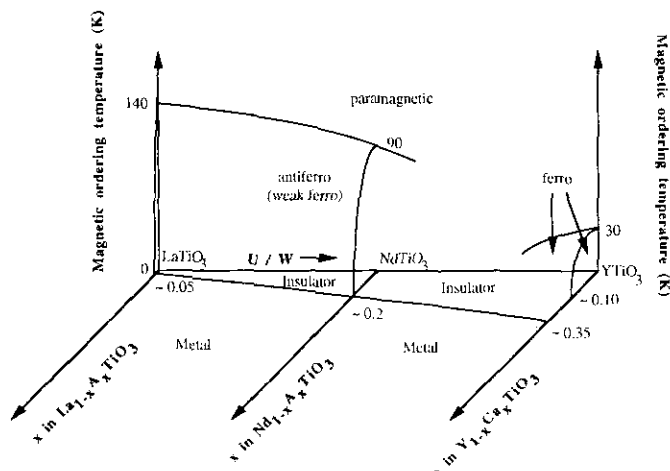
FIG. 10. Electronic and magnetic phase diagram of the $R_{1-x}A_xTiO_3$ series where R = La, Nd, Y and A = Ca, Sr, Ba. The magnetic ordering temperatures were plotted as a function of U/W ratio and hole concentration (x). The diagram is based on the model of Tokura (28).

$R_{1-x}A_xTiO_3$ series, where R = La, Nd, Y and A = Ca, Sr, Ba (see Fig. 10). $LaTiO_3$ can be viewed as a weakly correlated Mott insulator with a very small U/W ratio where U is Coulomb correlation energy and W is the one-electron band width (28). In contrast, $YTiO_3$ is proposed to be a strongly correlated insulator with a larger U/W ratio (28). The metal–insulator transition and the magnetic ordering seem to be related to each other in the $La_{1-x}A_xTiO_3$ (A = Sr, Ba) series where the substitution of a small percentage of A is sufficient to disrupt the antiferromagnetic ordering and cause metallic conductivity (6–9). However, strongly correlated $YTiO_3$ requires at least 35% Ca to induce metallic conductivity (10) but the disappearance of ferromagnetic ordering takes place at 10% Ca concentration. Thus, there appears to be no relationship between the metal–insulator transition and the magnetic ordering in the $Y_{1-x}Ca_xTiO_3$ system (10). We find that the magnetic ordering in the $Nd_{1-x}A_xTiO_3$ (A = Ca, Sr, Ba) systems disappears at approximately the same A concentrations as the onset of metallic behavior.

The transition metal oxygen bond distance M–O and the M–O–M bond angle are two important structural parameters that influence properties of the perovskite-like compounds. The relationship between transport properties and M–O distances has been well established. For example, the $Tl(Sr_{1-x}Ba_xLa)CuO_5$ series (2) shows a metal–insulator transition with increasing x without a structural phase transition. This metal–insulator transition is attributed to electron localization that results from lengthening of the Cu–O bonds when Ba^{2+} is substituted for Sr^{2+}. This bond elongation causes a narrowing of the x^2-y^2 (Cu–O σ^*) band and opens at band gap. The $RTiO_3$ series, however, are good examples of compounds whose

properties are mainly influenced by the M–O–M angle. The Ti–O distances are constant in the $RTiO_3$ series (Ti–O $\approx$ 2.03 Å); however, the Ti–O–Ti angles decrease (160° → 140°) with increasing orthorhombic distortion from La to Lu (4). The decrease in the Ti–O–Ti angle results in the narrowing of the Ti $3d$ bandwidth that in turn generates larger band gaps.

We find that the properties of the orthorhombic $Nd_{1-x}A_xTiO_3$ compounds are influenced by both Ti–O distance and Ti–O–Ti angle while the properties of the cubic samples are affected by the Ti–O distance. Therefore, we will discuss the orthorhombic and cubic samples individually.

The change in the average Ti–O distance as a function of x is plotted in Fig. 11 for the $Nd_{1-x}A_xTiO_3$ compounds where A = Sr, Ba. It was assumed that the distances decreased linearly with x for the orthorhombic phases. In the orthorhombic regions, the substitution of A^{2+} for Nd^{3+} increases the average ionic size at the Nd^{3+}/A^{2+} site that results in an increase in the Ti–O–Ti angle (decrease in the orthorhombic distortion). The Ti–O distance in this region is mainly influenced by the Ti^{3+}/Ti^{4+} ratio ($r_{Ti^{3+}}$ = 0.810 Å; $r_{Ti^{4+}}$ = 0.745 Å) and therefore decreases with increasing A^{2+} concentration. The increase in the Ti–O–Ti angle and the shortening of the Ti–O distance both increase the degree of metal–oxygen overlap and the bandwidth (W). Metal–insulator transitions occur at smaller x in the $Nd_{1-x}Ba_xTiO_3$ compounds (~10% Ba) than in the $Nd_{1-x}Sr_xTiO_3$ compounds (~20% Sr) as expected from these size considerations.

The Ti–O–Ti angle in the cubic ($Pm3m$) region is of course invariant. The average Ti–O distance (and W) is therefore affected by two competing structural factors; the Ti^{3+}/Ti^{4+} ratio and the effective size at the Nd^{3+}/A^{2+} site. The substitution of A^{2+} for Nd^{3+} increases the effective size at the Nd^{3+}/A^{2+} site (increasing the Ti–O dis-
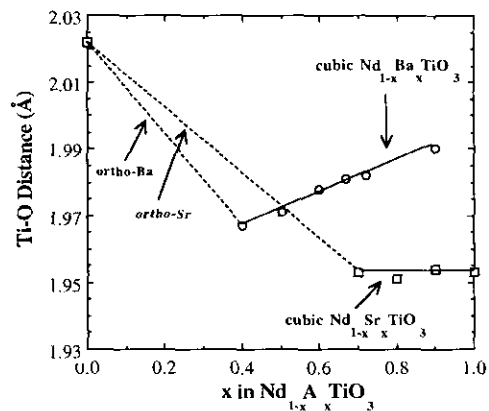

FIG. 11. Plots of Ti–O distances as a function of x in the $Nd_{1-x}A_xTiO_3$ (A = Sr, Ba) series. The Ti–O distance for $NdTiO_3$ was obtained from (4). The orthorhombic regions are represented by dashed lines.

tance) but decreases the size of the Ti^{3+}/Ti^{4+} site (decreasing the Ti–O distance). In the $Nd_{1-x}Sr_xTiO_3$ series, these factors offset each other and the Ti–O bond distances remain constant (see Fig. 11). In contrast, the Ba^{2+}/Nd^{3+} size disparity overrides the changing Ti^{3+}/Ti^{4+} ratio in the $Nd_{1-x}Ba_xTiO_3$ series and the Ti–O distances increase with x in the $Pm3m$ region. Increasing the Ti–O distance narrows the bandwidth and causes a M–I transition at $x \approx 0.72$. Because the Ti–O distance is invariant for the cubic $Nd_{1-x}Sr_xTiO_3$ compounds, metallic behavior persists up to $x \approx 0.95$. For example, $Nd_{0.1}Sr_{0.9}TiO_3$ shows metallic conductivity ($d_{Ti-O} = 1.954$ Å), whereas $Nd_{0.1}Ba_{0.9}TiO_3$ ($d_{Ti-O} = 1.990$ Å) is insulating.

We have excluded the $Nd_{1-x}Ca_xTiO_3$ system in the above discussion because there is not enough structural data to compare with the Sr and Ba systems. However, we do not anticipate a significant change in the Ti–O–Ti angle in this series because the average ionic size at the perovskite A site (Nd^{3+}/Ca^{2+}) does not vary significantly with Ca^{2+} ($r = 1.48$ Å) for Nd^{3+} ($r = 1.41$ Å) substitution. The Ti–O–Ti angle in $CaTiO_3$ (155.9°) (29) is only slightly larger than that in $NdTiO_3$ (150.5°) (4). In contrast, the Ti–O bond distances decrease with x (lowering of the Ti^{3+}/Ti^{4+} ratio) with end member distances of 1.956 Å ($CaTiO_3$) and 2.03 Å ($NdTiO_3$). Therefore, the properties of the $Nd_{1-x}Ca_xTiO_3$ are influenced primarily by the Ti–O distance. However, it is not clear why metal–insulator transitions occur at approximately the same x in the $Nd_{1-x}Ca_xTiO_3$ and the $Nd_{1-x}Sr_xTiO_3$ systems.

In the absence of sufficient structural data, attempts to accurately correlate transport properties to Ti–O distances and Ti–O–Ti angles are difficult. The perovskite tolerance factor, t, provides a rough estimate of the A–O/B–O bond mismatch and has been used to correlate structural parameters and instabilities in other systems (30–32). We have generated a sorting diagram based on tolerance factors in an attempt to separate metallic phases from insulating phases in the $R_{1-x}A_xTiO_3$ compounds (R = La, Nd, Y and A = Ca, Sr, Ba) as shown in Fig. 12. The tolerance factors used are purely steric and they do not take into account the electronic effects (e.g., orbital diffuseness, basicity) of the A-site cations. The band insulators $ATiO_3$ (A = Ca, Sr, Ba) have no carriers and of course are not expected to follow these criteria. Although rudimentary, this model adequately distinguishes metallic from insulating phases without the need of structural data.

The nature of the metal–insulator transitions in these types of materials is still subject to controversy. Our descriptions of the M–I transitions at both high and low carrier concentrations (or x values) are based on a Mott–Hubbard model. The M–I transitions for the rare-earth-rich phases described here appear to be of the Mott–Hubbard type in that the disappearance of magnetic
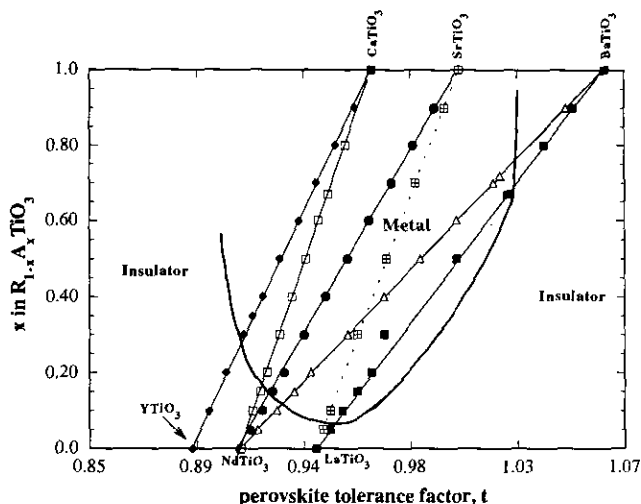

FIG. 12. The perovskite tolerance factors as a function of x in the $R_{1-x}A_xTiO_3$ series where R = La, Nd, Y and A = Ca, Sr, Ba.

ordering and the onset of metallic behavior seem to be linked. In the closely related $Y_{1-x}Ca_xTiO_3$ system (10), however, magnetic ordering and metallic behavior are independent and may be more complicated. We have also classified the M–I transitions in the cubic, alkaline-earth-rich regions of the $R_{1-x}Ba_xTiO_3$ phase diagrams (R = La, Nd, Y) as Mott–Hubbard types due to the strong relationships between the Ti–O distance and metallic behavior (33). For example, the insulating $La_{0.2}Ba_{0.8}TiO_3$ phase can be driven into the metallic state through Ca^{2+}-for-Ba^{2+} substitution ($La_{0.2}Ba_{0.6}Ca_{0.2}TiO_3$ is metallic) without changing the carrier concentrations (33). Although one cannot rule out Anderson-type localizations for these systems, the data are more consistent with Mott–Hubbard-type transitions.

SUMMARY

In summary, we have prepared three series of perovskite compounds $Nd_{1-x}A_xTiO_3$ (A = Ca, Sr, Ba) that show alkaline-earth-dependent metal–insulator and structural phase transitions. $NdTiO_3$ and the insulating $Nd_{1-x}A_xTiO_3$ compounds show weak ferromagnetic moments due to canted antiferromagnetic ordering at low temperatures. The onset of metallic behavior coincides with the disappearance of the magnetic ordering in the $Nd_{1-x}A_xTiO_3$ series. The transport properties of the orthorhombically distorted phases are influenced by the both Ti–O–Ti angles and the Ti–O distances whereas the properties of the cubic phases are affected by the Ti–O distances. We have also shown that a perovskite tolerance factor is a useful tool to sort metallic phases from insulating phases in the $R_{1-x}A_xTiO_3$ compounds where R = La, Nd, Y and A = Ca, Sr, Ba.

ACKNOWLEDGMENTS

REFERENCES

1. J. K. Burdett, *Inorg. Chem.* **32,** 3915 (1993).
2. M. A. Subramanian and M. H. Whangbo, *J. Solid State Chem.* **49,** 219 (1992).
3. J. Zaanen, G. A. Sawatzky, and J. W. Allen, *Phys. Rev. Lett.* **55,** 418 (1985).
4. D. A. Maclean, H.-K. Ng, and J. E. Greedan, *J. Solid State Chem.* **30,** 35 (1979).
5. J. E. Greedan, *J. Less-Common Metals* **111,** 335 (1985).
6. C. Eylem, G. S. Szabo, B. H. Chen, B. W. Eichhorn, J. L. Peng, R. Greene, L. Salamanca-Riba, and S. Nahm, *Chem. Mater.* **4,** 1038 (1992).
7. Y. Tokura, Y. Taguchi, Y. Okada, Y. Fujishima, T. Arima, K. Kumagai, and Y. Iye, *Phys. Rev. Lett.* **70,** 2126 (1993).
8. J. E. Sunstrom, S. M. Kauzlarich, and P. Klavins, *Chem. Mater.* **4,** 346 (1992).
9. J. E. Sunstrom and S. M. Kauzlarich, *Chem Mater.* **5,** 1539 (1993).
10. Y. Taguchi, Y. Tokura, T. Arima, and F. Inaba, *Phys. Rev. B* **48,** 511 (1993).
11. H. L. Ju, C. Eylem, J. L. Peng, B. W. Eichhorn, and R. L. Greene, *Phys. Rev. B,* **49,** 13 335 (1994).
12. J. E. Sunstrom, S. M. Kauzlarich, and M. R. Antonio, *Chem. Mater.* **5,** 182 (1993).
13. D. Pines and P. Nozieres, "The Theory of Quantum Liquids." Benjamin, New York, 1966.
14. A. V. Mahajan, D. C. Johnston, D. R. Torgeson, and F. Borsa, *Phys. Rev. B* **46,** 10973 (1992).
15. P. W. Anderson, *Phys. Rev.* **109,** 1492 (1958).
16. R. D. Shannon, *Acta Crystallogr. Sect. A* **32,** 751 (1976).
17. J. Wang, F. Guyot, A. Yeganeh-Haeri, and R. C. Liebermann, *Science* **244,** 468 (1990).
18. D. A. Crandles, T. Timusk, J. D. Garrett, and J. E. Greedan, *Physica C* **201,** 407 (1992).
19. J. D. Garrett, J. E. Greedan, and D. A. Maclean, *Mater. Res. Bull.* **16,** 145 (1981).
20. J. P. Goral and J. E. Greedan, *J. Magn. Magn. Mater.* **37,** 315 (1983).
21. (a) M. Kestigan and R. J. Ward, *J. Am. Chem. Soc.* **76,** 6027 (1954); (b) E. F. Bertaut and F. J. Forrat, *J. Phys. Radium* **17,** 129 (1956); (c) H. Holzapfel and J. Sieler, A. *Anorg. Allg. Chem.* **343,** 174 (1966); (d) P. Ganguly, O. Parkash, and C. N. R. Rao, *Phys. Status Solidi A* **36,** 669 (1976).
22. (a) H. L. Yakel, *Acta Crystallogr.* **8,** 394 (1955); (b) S. Geller, *Acta Crystallogr.* **10,** 243 (1957); (c) P. Dougier and P. Hagenmuller, *J. Solid State Chem.* **11,** 177 (1974); (d) P. Dougier, D. Deglane, and P. Hagenmuller, *J. Solid State Chem.* **19,** 135 (1976); (e) P. Bordet, C. Chaillout, M. Marezio, Q. Huang, A. Santoro, S.-W. Cheong, H. Takagi, C. S. Oglesby, and B. Batlogg, *J. Solid State Chem.* **106,** 253 (1993).
23. M. Ceh, D. Kolar, and L. Golic, *J. Solid State Chem.* **68,** 68 (1987).
24. D. A. Maclean, K. Seto, and J. E. Greedan, *J. Solid State Chem.* **40,** 241 (1981).
25. J. E. Greedan, *J. Magn. Magn. Mater.* **44,** 299 (1984).
26. D. A. Maclean and J. E. Greedan, *Inorg. Chem.* **20,** 1025 (1981).
27. F. Lichtenberg, D. Widmer, J. G. Bednorz, T. Williams, and A. Reller, *Z. Phys. B* **82,** 211 (1991).
28. Y. Tokura, *J. Phys. Chem. Solids* **53,** 1619 (1992).
29. H. J. A. Koopmans, G. M. H. Van de Velde, and P. J. Gellings, *Acta Crystallogr. Sect. C* **39,** 1323 (1983).
30. J. F. Bringley, S. S. Trail, and B. A. Scott, *J. Solid State Chem.* **86,** 310 (1990).
31. B. H. Chen and B. W. Eichhorn, *J. Solid State Chem.* **97,** 340 (1992).
32. C. N. R. Rao and J. Gopalakrishnan, "New Directions in Solid State Chemistry." Cambridge Univ. Press, 1986.
33. C. Eylem, Ph.D. Thesis, University of Maryland, College Park, 1994.